HHS Public Access

Author manuscript

*Ultrasound Med Biol*. Author manuscript; available in PMC 2017 April 11.

Published in final edited form as:

*Ultrasound Med Biol*. 2016 August ; 42(8): 1986–1997. doi:10.1016/j.ultrasmedbio.2016.03.004.

# IMPROVING DISPLACEMENT SIGNAL-TO-NOISE RATIO FOR LOW-SIGNAL RADIATION FORCE ELASTICITY IMAGING USING BAYESIAN TECHNIQUES

**Douglas M. Dumont**, **Kristy M. Walsh**, and **Brett C. Byram**

Department of Biomedical Engineering, Vanderbilt University, Nashville, TN, USA

## Abstract

Radiation force-based elasticity imaging is currently being investigated as a possible diagnostic modality for a number of clinical tasks, including liver fibrosis staging and the characterization of cardiovascular tissue. In this study, we evaluate the relationship between peak displacement magnitude and image quality and propose using a Bayesian estimator to overcome the challenge of obtaining viable data in low displacement signal environments. Displacement data quality were quantified for two common radiation force-based applications, acoustic radiation force impulse imaging, which measures the displacement within the region of excitation, and shear wave elasticity imaging, which measures displacements outside the region of excitation. Performance as a function of peak displacement magnitude for acoustic radiation force impulse imaging was assessed in simulations and lesion phantoms by quantifying signal-to-noise ratio (SNR) and contrast-to-noise ratio for varying peak displacement magnitudes. Overall performance for shear wave elasticity imaging was assessed in *ex vivo* chicken breast samples by measuring the displacement SNR as a function of distance from the excitation source. The results show that for any given displacement magnitude level, the Bayesian estimator can increase the SNR by approximately 9 dB over normalized cross-correlation and the contrast-to-noise ratio by a factor of two. We conclude from the results that a Bayesian estimator may be useful for increasing data quality in SNR-limited imaging environments.

### Keywords

Displacement estimation; Elasticity imaging; Shear wave; Bayes; Medical imaging; Elastography; Ultrasound

## INTRODUCTION

Radiation force-based elasticity imaging describes a group of ultrasonic techniques that estimate the elastic properties of underlying tissue structures based on their response to acoustic radiation force (ARF). The tissue mechanical response to the ARF-induced deformation is generally observed spatially and temporally using conventional ultrasonic pulses (Doherty et al. 2013b; Gennisson et al. 2013; Nightingale 2011; Sarvazyan et al.

Address correspondence to: Brett C. Byram, PMB 351631, Nashville, TN, 37235, USA. brett.c.byram@vanderbilt.edu.

1998). These data are then used to either form a displacement image showing the relative stiffness of tissue structures (*i.e.*, acoustic radiation force impulse imaging [ARFI]) or input into a mechanical model to extract quantitative mechanical tissue properties (*i.e.*, shear wave elasticity imaging, wherein shear moduli values are derived from measurements of shear wave velocity) (Nightingale et al. 2001; Sarvazyan et al. 1998). ARF-derived metrics have been proposed by several groups as potential imaging biomarkers for staging liver fibrosis (Deffieux et al. 2015; Palmeri et al. 2011; Urban et al. 2012; Zhao et al. 2014); characterizing cervical, breast and prostate tissue (Athanasiou et al. 2015; Carlson et al. 2014; Muller et al. 2015; Palmeri et al. 2015; Zhai et al. 2012); staging kidney disease (Samir et al. 2015; Urban et al. 2012); characterizing cardiovascular disorders (Czernuszewicz et al. 2015; Scola et al. 2012; Doherty et al. 2015); and monitoring and guiding radiofrequency (RF) ablations in cardiac tissue (Eyerly et al. 2015; Bahnson et al. 2014).

It is not surprising that the quality of these techniques is dependent in part on the quality of the ARF-induced displacement estimates. Physiological motion (Fahey et al. 2007), speckle-bias (Elegbe and McAleavey 2013; Menon et al. 2010), thermal noise, finite spatial and temporal resolution and finite signal bandwidth all limit achievable displacement accuracy (Walker and Trahey 1995). Additionally, peak ARF-induced displacement is limited by increased attenuation (*i.e.*,by absorbing and shifting the peak signal shallow to the region-of-interest [Palmeri et al. 2005; Palmeri and Nightingale 2011]), by regulatory limits on acoustic output (*i.e.*, mechanical index) or thermal bioeffects (Deng et al. 2015; Dhanaliwala et al. 2012; Liu et al. 2014) or, in the case of shear wave elasticity imaging, by the geometric spreading and absorption of the shear wave as it propagates (Parker and Baddour 2014; Sarvazyan et al. 1998). In viscous tissue, increased shear wave attenuation due to dispersion can further decrease displacement magnitude (Parker and Baddour 2014), potentially limiting the distance the propagating shear wave can be successfully observed. Limitations in achievable displacement signal-to-noise ratio (SNR) due to limitations in achievable displacement signal magnitude can impact the depth-of-penetration of these techniques (Palmeri and Nightingale 2011), the percent yield of viable or ARF-derived measurements (Deng et al. 2015).

Previously, we proposed using Bayesian-based displacement estimation to improve the tracking of small displacements, and found that the estimator could reduce the mean-square error of the displacement estimate by approximately an order of magnitude over a traditional correlation-based estimator (Byram et al. 2013a, 2013b; Dumont and Byram 2016). Our prior investigation quantified the performance in a mean-square error sense in the context of thermal noise and shearing-induced decorrelation solely for ARFI imaging, whereas here we investigate the recovery of data quality in low displacement scenarios at the initial on-axis excitation site and after attenuation due to shear wave propagation (Dumont and Byram 2016).

In this work, we investigate the ability of the previously described Bayesian estimator to improve the displacement SNR in the scenario in which displacement magnitude is limited in some way, either by the physical characteristics of the tissue itself or by limitations on the radiation force that can be achieved by the system. While there are many potential factors

that can limit the amount of ARF generated for a given depth *in vivo* (*e.g.*, absorption along the propagation path, increased attenuation, target depth, aberration of the excitation beam, *etc.*), we make the simplifying assumption herein that the end result of all these factors is low displacement signal in the form of low displacement magnitude.

This paper is organized as follows. First, we review the proposed Bayesian estimator. Next, we describe simulation, phantom and *ex vivo* experiments quantifying performance as a function of decreasing displacement magnitude and compare the results of the Bayesian estimator with that of a traditional, normalized cross-correlation (NCC) estimator. Finally, we summarize the data and discuss directions for improvement.

## MATERIALS AND METHODS

### Bayesian estimation of ARF-induced displacements

The tracking of small displacements using Bayesian techniques has been described previously (refer to our earlier work for more detail: Byram et al. 2013a, 2013b; Dumont and Byram 2016). Briefly, the Bayesian estimator maximizes the global log-posterior probability between a given set of displacement estimates and the corresponding RF reference-track paired data. The log-posterior probability $P_k(\tau_k/x)$ is computed as the following summation:

$$ln(P_k(\tau_k|\,x)) \propto ln(P_k(x|\tau_k))+ln(P_k(\tau_k)), \quad (1)$$

which gives the log-posterior probability of the displacement estimate $\tau_k$ for kernel $k$ given the log-likelihood, $ln(P_k(x/\tau_k))$ and the log-prior $ln(P_k(\tau_k))$ (Dumont and Byram 2016). The log-likelihood is given by:

$$ln(P_k(x|\tau_k))= -\frac{1}{4\sigma_n^2}\sum_{n=0}^{M-1}(s_1[n]-s_2[n;-\tau_k])^2, \quad (2)$$

which evaluates the likelihood of obtaining data $x$, taken here to be some reference RF signal $s_1$ (containing $n$ samples indexed over kernel-length $M$) after undelaying the tracked RF signal $s_2$ by $-\tau_k$ (Carlson and Sjoberg 2004; Dumont and Byram 2016). Parameter $\sigma_n$ characterizes the quality of the tracked RF data and is derived from a peak correlation coefficient-derived estimation of the SNR, which captures both thermal noise and tissue decorrelation based signal distortions (Byram et al. 2013b; Dumont and Byram 2016). Additional information is incorporated into the problem in the form of a generalized Gaussian Markov random field prior:

$$ln(P_k(\tau_k))= -\frac{1}{p\lambda^p}\sum_{k,j\in B} w_j|\tau_k-\tau_j|^p \quad (3)$$

where $\tau_j$ are displacement estimates located within a neighborhood that is spatially adjacent to the current estimate $\tau_k$. The terms $\lambda$ and $p$ are tuning parameters that control the degree to which additional information is combined with the log-likelihood and the extent to which edges are preserved within the displacement field (Bouman and Sauer 1993; Dumont and Byram 2016). More specifically, $p$ is a continuous shape parameter with classic cases at $p$ = 2 (Gaussian distribution) and $p$ = 1 (Laplace distribution), which determine how uniformly variations in displacement through depth are penalized. The $\lambda$ parameter controls the width of these distributions. For this work, the method is implemented in the axial dimension and estimates immediately adjacent to the current estimate are used as the source of additional information (Dumont and Byram 2016). The absolute value term in the prior is approximated by $\left(\sqrt{((\tau_0-\tau_j)^2+\varepsilon)}\right)^p$, $\varepsilon$=$10^{-6}$ (Lee et al. 2006; Dumont and Byram 2016). The negative of eqn (1) is then summed axially over the region-of-interest and is solved as a minimization problem to find the vector of displacement estimates producing the largest global log-posterior probability (*i.e.*, the smallest global negative log-posterior probability). The non-linear minimization was implemented in MATLAB (The Mathworks Inc., Natick, MA, USA) using the unconstrained minimization routine fminunc, and the optimization was run until reaching a user-specified number of iterations (1000) or a convergence tolerance on the cost function or the parameter values. (In MATLAB these parameters are TolX and TolFun, respectively, and they were both left at the default value of $10^{-6}$).

## Simulations

Previously described techniques were used to create finite element models of ARF-induced displacements combined with Field II simulations modeling the tracking of displacement fields in a 6.5 kPa homogeneous medium. (Jensen 1996; Jensen and Svendsen 1992; Palmeri et al. 2005, 2006). In the tracking portion of the simulation, a scatterer density greater than 15 scatterers/resolution cell was used to ensure fully developed speckle throughout the simulated field.

To investigate the relationship between displacement magnitude and estimator performance, the load-curve of the excitation source was scaled to produce a range of peak displacements of approximately 0.3–17 $\mu$m. Twenty-five independent speckle realizations were then simulated for each displacement magnitude. The simulated and tracked RF data were then corrupted with additive white Gaussian noise to produce a SNR of 30 dB. Table 1 lists the parameters used for the simulations and the Bayesian and NCC estimators.

Displacement SNR was then measured for each dataset as

$$SNR=\frac{\mu^2}{MSE} \quad (4)$$

where $\mu$ represents the mean displacement at a given axial location, averaged over every realization, and *MSE* represents the mean-square error between the realization being analyzed and the mean NCC displacement averaged over every realization except the one

being analyzed. Displacement SNR was then quantified as a function of time after the excitation.

## Lesion visualization experiments

To investigate the impact of decreasing displacement magnitude on lesion visualization for ARFI imaging, a custom tissue-mimicking lesion phantom (CIRS, Norfolk, VA, USA) was imaged with ARF using the Verasonics Vantage 128 Research scanner (Verasonics Inc., Redmond, WA, USA) and the L7-4 linear transducer. Two lesions were imaged: a 21-kPa 10-mm spherical lesion and a 45-kPa 10-mm spherical lesion embedded in a homogenous 6.5-kPa background. ARFI 2-D images were created by translating the excitation beam electronically across a 3-cm field of view. The phantom response to the ARF was monitored using plane wave insonification at a pulse-repetition frequency of 6.7 kHz. Displacement magnitude was varied by adjusting the pulse-length of the excitation pulse (10–192 $\mu s$) to produce a range of peak displacements within the phantom. The range of excitation lengths are all shorter than the duration required for the shear wave to propagate beyond the spatial extent of the excitation, which means that the varied pulse lengths should have a relatively minimal impact on the frequency content of the shear wave (Nightingale 2011). Specifically, the propagation duration of the shear wave in the stiffest material (45-kPa lesion) within the region of excitation is 238 ms compared to the longest excitation pulse of 192 ms. Table 2 lists the parameters used to generate and process the displacement data for each estimator. Displacement data were motion filtered to remove any non-ARF-induced motion (Giannantonio et al. 2011) and then formed into 2-D qualitative ARFI displacement images.

Quantitative imaging performance was evaluated for each estimator as a function of displacement magnitude by measuring the contrast and contrast-to-noise ratio (CNR) between a 0.8-cm circle centered within each lesion and one located at the same depth but offset into the phantom background. The same regions were used for both estimators. Contrast and CNR were quantified for each dataset as

$$\text{Contrast}=\frac{\mu_o-\mu_i}{\mu_o}, \text{and} \quad (5)$$

$$CNR=\frac{|\mu_o-\mu_i|}{\sqrt{\sigma_o^2+\sigma_i^2}}, \quad (6)$$

where $\mu_i$, $\mu_o$, $\sigma_i^2$ and $\sigma_o^2$ are the displacement mean and variance inside and outside the lesion, respectively.

## Shear wave experiments

Next, we examined SNR differences during shear wave propagation. Shear wave displacement amplitudes decrease during propagation due to both geometric spreading, as well as losses in dispersive media (Parker and Baddour 2014; Sarvazyan et al. 1998).

Estimation performance as a function of distance from the excitation source was quantified in samples of fresh chicken breast (Kroger Foods, Nashville, TN, USA), using the Verasonics Vantage 128 Research scanner and the L7-4 linear transducer. Chicken breast was chosen due to its increased shear viscosity over conventional gelatin phantoms (Qiang et al. 2011). Each chicken breast sample (n = 6) was degassed in a vacuum chamber, positioned underneath the transducer and acoustically coupled to the array with gel. Shear wave datasets were acquired by exciting the sample with ARF (using the same excitation parameters described in Table 2, but with a single excitation using a pulse length of 192 $\mu$s), and then tracking the propagating shear wave using a plane-wave transmit sequence at a pulse repetition frequency of 6.7 kHz. Based on the size of the sample, two to three sites were imaged per chicken breast for a total of 16 measurements.

Displacement data were then motion-filtered using the interpolative regression method to minimize non-ARF-induced motion (Giannantonio et al. 2011). Due to the possibility of the variability between samples, the displacement SNR was quantified differently than with the simulation data. First, an estimate of the signal power was computed by taking a 1-D moving average of the axial displacement data for each estimator (3-mm kernel) and then integrating the square of this average signal over the same size kernel. Next, an estimate of the noise power was computed by taking a 1-D moving average of the axial displacement data (3-mm kernel) estimated using NCC and then subtracting this average NCC signal from the displacement profile calculated by each estimator. These data were then integrated over the same sized kernel and squared. Finally, the SNR was calculated as the ratio of the signal power to the noise power, and was converted to dB.

The SNR was then quantified as a function of both space and time in 3-mm region near the excitation focus (22–25 mm) along a trajectory defining the propagation path of the traveling shear wave. The most likely trajectory of the shear wave was determined using the Bayesian displacement data and the Radon-sum method proposed by Rouze et al. (2010). The same trajectory was used to evaluate the SNR for both methods for a given dataset.

## RESULTS

Figure 1 shows the axial displacement of the peak time-step for every speckle realization as a function of decreasing displacement magnitude. Figures 1a–1d show the results for the normalized cross correlation estimator, while Figures 1e–1h show the corresponding results when using the Bayesian estimator. Each image is scaled to the show the central 90th percentile of the displacement data (*i.e.*, the 5th–95th percentile), while the title for each sub-figure lists the corresponding peak displacement from the finite element simulation. The results suggest the qualitative performance for NCC is maintained when the displacement magnitude is decreased to approximately 5 $\mu$m, followed by a noticeable drop off in quality at approximately 1 $\mu$m, where the variability within the measurement makes resolving the true displacement profile challenging. At 0.3 $\mu$m, the NCC displacement profile is almost completely masked by the measurement noise. In contrast, the Bayesian data show much less variability at all displacement magnitudes, with little drop-off in quality until 1 $\mu$m. At 0.3 $\mu$m, the Bayesian estimator begins to noticeably suffer, only partially recovering the underlying displacement profile across realizations.

Figure 2 shows how the SNR changes as a function of the displacement magnitude for the peak-displacement time-step (t = 0.6 ms following the excitation). The results show that the Bayesian estimator improves the displacement SNR by an average of 8.9 dB (range 7.7–10.9 dB) over NCC. The data also suggest that with the Bayesian estimator, displacement magnitudes can be reduced by almost one-half to one order of magnitude without a significant loss of SNR performance relative to NCC. Figure 2 also demonstrates the average decorrelation experienced at the peak focal displacement as a function of peak displacement magnitude. These results are shown for several levels of thermal noise in order to provide context for when shearing or thermal noise- induced decorrelation are the dominant mechanisms of decorrelation. Thermal noise dominant decorrelation can be identified because it is independent of peak displacement, whereas shearing-induced decorrelation scales with the peak magnitude. The no added noise case (Inf dB) is shown to demonstrate the trend without any thermal noise-induced decorrelation. Figure 3 shows how the SNR changes for both estimators as a function of time following the excitation. The data suggest that the improvement in SNR when using the Bayesian estimator is maintained up to and beyond the peak displacement time-step. Finally, for context we report run times of NCC and the Bayes method applied to peak ARF-induced displacements using our MATLAB implementations. The NCC and Bayesian algorithms required 0.16 ± 0.00047 s and 0.44 ± 0.052 s, respectively. We do not suggest that either of these are optimally implemented in MATLAB, but it demonstrates approximate trends in run time between the two algorithms.

Figures 4 and 5 show representative lesion phantom images for both estimators as a function of displacement magnitude and excitation pulse length: 192 $\mu$s (a), 96 $\mu$s (b), 19 $\mu$s (c) and 10 $\mu$s (d), respectively. The results illustrate both the loss of image quality and the decrease in the visibility of the lesion as displacement magnitude and thus signal strength are gradually reduced. The NCC images suggest that image quality does not noticeably change until the peak displacements in the background region fall below 1 $\mu$m, at which point the variability of the measurement begins to significantly reduce the visibility of the lesion. For the shortest excitation pulse length (column d), the lesion is almost impossible to distinguish from the measurement noise in the NCC image. The Bayesian images show much less variability and greater apparent lesion contrast at all displacement magnitudes. The lesion is still visible in the Bayesian images when the excitation burst length is reduced to 19 $\mu$s (column c), and is partially visible for the smallest displacement magnitude (column d).

Figure 6 shows the lesion contrast and CNR as a function of increasing displacement magnitude. The results show that for any given displacement magnitude level, the Bayesian estimator can double the CNR while still maintaining contrast. The results also illustrate a gradual decrease in CNR with decreasing displacement for both estimators down to approximately 1–2 $\mu$m, at which point the CNR falls off rapidly as displacement magnitudes are further reduced. The results also illustrate how much the displacement magnitudes can be reduced when using a Bayesian estimator while still maintaining similar CNR performance as NCC. As expected, the contrast—primarily related to the imaging system and the material properties—does not change between the two approaches (Nightingale et al. 2006).

Figures 7a and 7b show displacement data computed by each estimator from a single chicken breast sample as a function of time and distance from the excitation source for a point located at the focus. The solid white lines show the corresponding time-of-flight trajectory estimated by the Radon-sum transformation of the Bayesian data used in the SNR analysis (Rouze et al. 2010). Figure 7c shows displacement versus distance from the excitation source for data points located along the time-of-flight trajectory of the propagating shear wave. These data have been normalized to the peak displacement located at the very center of the excitation source. Each gray data point shows the relative displacement for each measurement site, while the black line shows the mean relative displacement as a function of distance from the excitation source, averaged over every sample (n = 16 measurement sites, 2–3 sites per chicken breast sample). The dashed lines show the region chosen for the signal-to-noise analysis. The first dashed line defines a point that lies outside the region-of-excitation where a shear wave is first clearly observed within the data, while the second dashed line represents the point where the relative displacement (relative to the first dashed line) falls below 10% of its initial value.

Figure 8 shows the SNR for the chicken breast data as a function of distance from the excitation source. The SNR is calculated over a 3-mm region below the excitation focus and represents the SNR for the data that lies along the time-of-flight trajectory of the propagating shear wave; the error bars show the mean and standard error of the mean of the data over the 16 measurement sites. These data show that the Bayesian estimator gives an average improvement of 8.5 dB in displacement SNR (range, 2.6–11.9 dB) over NCC and that this improvement is largely maintained throughout the analysis region. These data show that for an NCC estimator, the displacement SNR associated with the peak of the propagating shear wave falls to approximately 0 dB within 7 mm, while the mean displacement SNR for the Bayesian estimator falls to approximately 5 dB within the same distance. If a cut-off value of 5 dB is chosen as the magnitude in which a shear wave is successfully detected, the Bayesian estimator—at least within this dataset—is able to track the shear wave peak approximately twice as far in a dispersive media.

## DISCUSSION

The results illustrate the degradation in displacement SNR that occurs with decreasing displacement magnitude in ARF-based imaging and demonstrate the ability of a Bayesian-based estimator to improve SNR relative to NCC, even as signal strength is gradually decreased. Figure 2 shows that the SNR for both estimators increases at a logarithmic rate up to 10 $\mu$m, at which point the SNR begins to plateau to approximately 17 dB for the NCC estimator and 25 dB for the Bayesian estimator. Our peak NCC SNR results are consistent with simulation work performed by Dhanaliwala et al. (2012), who reported SNRs of approximately 20 dB for simulated ARF-induced displacements greater than 10 $\mu$m, when using the Loupas autocorrelator and a 1-D transducer. Our NCC SNR results are also similar to the results reported by Dhanaliwala et al. (2012) for peak displacement magnitudes less than 1 $\mu$m, where the displacement SNR is observed to fall below 0 dB. Overall, our data suggest that for any given displacement magnitude level, the Bayesian estimator can improve the SNR by approximately 8–9 dB over a conventional NCC estimator.

The trend in SNR with respect to displacement magnitude illustrates the complex relationship that shearing-induced decorrelation, speckle bias and the limitations imposed by the finite spatial resolution, temporal resolution, bandwidth and sampling capabilities of ultrasound have on the performance of any ARF-based displacement estimator. At relatively high displacement signal strength (*i.e.*, >10 $\mu$m), the SNR is bounded by the shearing-induced decorrelation, whereas at relatively low displacement signal strength, the SNR is dominated by the lower bound on the variance of the measurement jitter due to the signal and resolution limitations of ultrasound (Palmeri et al. 2006; Walker and Trahey 1995). In other words, decreasing the ARF displacement magnitude does result in decreased noise power of the NCC estimates, but the end result is still a lower displacement estimation SNR due to the inherent limitations of the imaging system (Walker and Trahey 1995).

Our results suggest that SNR of the Bayesian estimator follows a similar trend with respect to displacement magnitude, which is not surprising given that the noise model for the likelihood is estimated from the NCC coefficient between the time-shifted signals. Even though the Bayesian estimator has been demonstrated to have superior performance in terms of measurement variance (Dumont and Byram 2016), this work suggests that the improvement in variance performance is not enough to completely offset the loss in signal as displacement magnitudes are reduced. It is possible that our assumption—that a peak correlation coefficient-derived noise metric can completely model the noise inherent to the estimation task—becomes less appropriate at very low displacements, where the lack of significant decorrelation results in high correlation coefficients, which may not be representative of the true measurement variance associated with measuring sub-micron displacements. It is also possible that our likelihood function—which is a sum-square difference between the time-shifted signals—also bounds the performance. It is likely that even better performance could be realized with a different noise model or a function that can more accurately estimate the likelihood associated with sub-micron time-shifts. Additionally, this study uses conventional ultrasound to estimate the ARF-induced displacements. Combining harmonic imaging tracking techniques with the Bayesian estimator may result in further improvements in SNR (Doherty et al. 2013a).

Figures 2, 4, 5, 6 and 7 demonstrate the most important result from this study, which is that viable ARF-based displacement data can be acquired with only a few microns of displacement when using the Bayesian estimator, and the dB improvement is maintained even for very low displacement signals (*i.e.*, <1 $\mu$m). For ARF-based applications that may be SNR-limited, such as shear wave elasticity imaging in deep visceral organs (Deng et al. 2015; Palmeri and Nightingale 2011), we hypothesize the increase in displacement SNR achieved by a Bayesian estimator will translate to an increase in the spatial extent of viable data (both in depth and away from the excitation) that can be used for the elastic modulus reconstruction, likely improving the yield of viable measurements. Figures 4, 5 and 6 suggest that viable ARF-based imaging data can be acquired with significantly shorter excitation burst lengths when using a Bayesian estimator. For ARF-based applications that are not necessarily SNR-limited, we hypothesize that a Bayesian estimator can be combined with lower intensity or lower excitation pulse lengths to acquire displacement data with similar SNR or CNR as NCC but at higher frame rates.

There are a number of other advanced algorithms for motion estimation, and a broad overview primarily focused on advances for large tissue deformation has recently been provided by De Luca et al (2015). For RF-based block matching approaches, other advanced algorithms have been proposed primarily to address problems encountered in quasi-static elastography (Chen et al. 2010; Jiang and Hall 2007; Zahiri-Azar and Salcudean 2006). In the case of static elastography, peak-hopping is a significant concern, so schemes to constrain the displacement field in a gross sense are important (Petrank et al. 2009). These methods are primarily interested in recovering Cramer-Rao bound limited estimates.

While it is possible that these schemes could be implemented in a manner that surpasses the Cramer-Rao lower bound in an overall mean squared error sense, this has not been demonstrated in the literature. Others have implemented regularized displacement estimators that constrain the solution based on various metrics, including the derivative (Chen et al. 2010; Pellot-Barakat et al. 2004; Rivaz et al. 2008). This may have advantages over our solution, and a derivative based constraint could still be implemented within our Bayesian framework. Finally, our approach most appropriately scales the data based on an adaptive measure of the signals noise power. Chen et al. (2010) scales the data term in their lateral regularization constraint by $\rho/1-p$, which is similar to our approach, but they do not correct for the local power in the RF signal. For the ARF-induced displacement estimation task, correctly scaling the data term (*i.e.*, the likelihood function) through depth is crucial to achieving better displacement estimates.

## CONCLUSIONS

We have presented a study investigating the relationship between displacement magnitude for ARF-based applications and SNR for a correlation-based estimator and a Bayesian-based estimator. SNR performance was quantified in simulation, phantom and *ex vivo* tissue samples. The results demonstrate that significant improvement in SNR can be achieved with a Bayesian estimator, even for low-magnitude displacements.

## Acknowledgments

We would like to thank Dr. Kathryn Nightingale for her valuable insight into this work. We would also like to thank the Advanced Computing Center for Research and Education (ACCRE) at Vanderbilt University, Nashville, TN, for computational support. This work was funded in part by NIH S10 1S10RR026828.

## References

Athanasiou A, Latorre-Ossa H, Criton A, Tardivon A, Gennisson JL, Tanter M. Feasibility of imaging and treatment monitoring of breast lesions with three-dimensional shear wave elastography. Ultraschall Med. 2015 Epub ahead of print.

Bahnson TD, Eyerly SA, Hollender PJ, Doherty JR, Kim YJ, Trahey GE, Wolf PD. Feasibility of near real-time lesion assessment during radiofrequency catheter ablation in humans using acoustic radiation force impulse imaging. J Cardiovasc Electrophysiol. 2014; 25:1275–1283. [PubMed: 25132292]

Bouman C, Sauer K. A generalized gaussian image model for edge-preserving map estimation. IEEE Trans Image Process. 1993; 2:296–310. [PubMed: 18296219]

Byram B, Trahey GE, Palmeri M. Bayesian speckle tracking. Part I: An implementable perturbation to the likelihood function for ultrasound displacement estimation. IEEE Trans Ultrason Ferroelectr Freq Control. 2013a; 60:132–143. [PubMed: 23287920]

Byram B, Trahey GE, Palmeri M. Bayesian speckle tracking. Part II: Biased ultrasound displacement estimation. IEEE Trans Ultrason Ferroelectr Freq Control. 2013b; 60:144–157. [PubMed: 23287921]

Carlson, J., Sjoberg, F. Simultaneous maximum likelihood estimation of time delay and time scaling. Proceedings of the 6th Nordic Signal Processing Symposium - NORSIG; June 9–11, 2004; IEEE, Espoo, Finland. p. 260-263.

Carlson LC, Feltovich H, Palmeri ML, del Rio AM, Hall TJ. Statistical analysis of shear wave speed in the uterine cervix. IEEE Trans Ultrason Ferroelectr Freq Control. 2014; 61:1651–1660. [PubMed: 25392863]

Chen L, Housden RJ, Treece GM, Gee AH, Prager RW. A hybrid displacement estimation method for ultrasonic elasticity imaging. IEEE Trans Ultrason Ferroelectr Freq Control. 2010; 57:866–882. [PubMed: 20378449]

Czernuszewicz TJ, Homeister JW, Caughey MC, Farber MA, Fulton JJ, Ford PF, Marston WA, Vallabhaneni R, Nichols TC, Gallippi CM. Non-invasive *in vivo* characterization of human carotid plaques with acoustic radiation force impulse ultrasound: Comparison with histology after endarterectomy. Ultrasound Med Biol. 2015; 41:685–697. [PubMed: 25619778]

De Luca V, Szkely G, Tanner C. Estimation of large-scale organ motion in b-mode ultrasound image sequences: A survey. Ultrasound Med Biol. 2015; 41:3044–3062. [PubMed: 26360977]

Deffieux T, Gennisson JL, Bousquet L, Corouge M, Cosconea S, Amroun D, Tripon S, Terris B, Mallet V, Sogni P, Tanter M, Pol S. Investigating liver stiffness and viscosity for fibrosis, steatosis and activity staging using shear wave elastography. J Hepatol. 2015; 62:317–324. [PubMed: 25251998]

Deng Y, Palmeri ML, Rouze NC, Rosenzweig SJ, Abdelmalek MF, Nightingale KR. Analyzing the impact of increasing mechanical index and energy deposition on shear wave speed reconstruction in human liver. Ultrasound Med Biol. 2015; 41:1948–1957. [PubMed: 25896024]

Dhanaliwala AH, Hossack JA, Mauldin FW. Assessing and improving acoustic radiation force image quality using a 1.5-d transducer design. IEEE Trans Ultrason Ferroelectr Freq Control. 2012; 59:1602–1608. [PubMed: 22828855]

Doherty JR, Dahl JJ, Trahey GE. Harmonic tracking of acoustic radiation force-induced displacements. IEEE Trans Ultrason Ferroelectr Freq Control. 2013a; 60:2347–2358. [PubMed: 24158290]

Doherty JR, Trahey GE, Nightingale KR, Palmeri ML. Acoustic radiation force elasticity imaging in diagnostic ultrasound. IEEE Trans Ultrason Ferroelectr Freq Control. 2013b; 60:685–701. [PubMed: 23549529]

Doherty J, Dahl J, Kranz P, El Husseini N, Chang HC, Chen NK, Allen J, Ham K, Trahey G. Comparison of acoustic radiation force impulse imaging derived carotid plaque stiffness with spatially registered MRI determined composition. IEEE Trans Med Imaging. 2015; 34:2354–2365. [PubMed: 25974933]

Dumont DM, Byram BC. Robust tracking of small displacements with a Bayesian estimator. IEEE Trans Ultrason Ferroelectr Freq Control. 2016; 63:20–34. [PubMed: 26529761]

Elegbe EC, McAleavey SA. Single tracking location methods suppress speckle noise in shear wave velocity estimation. Ultrason Imaging. 2013; 35:109–125. [PubMed: 23493611]

Eyerly SA, Vejdani-Jahromi M, Dumont DM, Trahey GE, Wolf PD. The evolution of tissue stiffness at radiofrequency ablation sites during lesion formation and in the peri-ablation period. J Cardiovasc Electrophysiol. 2015; 26:1009–1018.

Fahey BJ, Palmeri ML, Trahey GE. The impact of physiological motion on tissue tracking during radiation force imaging. Ultrasound Med Biol. 2007; 33:1149–1166. [PubMed: 17451869]

Gennisson JL, Deffieux T, Fink M, Tanter M. Ultrasound elastography: Principles and techniques. Diagn Interv Imaging. 2013; 94:487–495. [PubMed: 23619292]

Giannantonio DM, Dumont DM, Trahey GE, Byram BC. Comparison of physiological motion filters for *in vivo* cardiac ARFI. Ultrason Imaging. 2011; 33:89–108. [PubMed: 21710825]

Jensen JA. Field: A program for simulating ultrasound systems. Med Biol Eng Comput. 1996; 4(Suppl 1):351–353.

Jensen JA, Svendsen NB. Calculation of pressure fields from arbitrarily shaped, apodized, and excited ultrasound transducers. IEEE Trans Ultrason Ferroelec Freq Contr. 1992; 39:262–267.

Jiang J, Hall TJ. A parallelizable real-time motion tracking algorithm with applications to ultrasonic strain imaging. Phys Med Biol. 2007; 52:3773–3790. [PubMed: 17664576]

Lee, SI., Lee, H., Abbeel, P., Ng, AY. Efficient l1 logistic regression. Proceedings of the Twenty-First National Conference on Artificial Intelligence (AAAI-06); AAAI, Boston, MA. 2006;

Liu Y, Herman BA, Soneson JE, Harris GR. Thermal safety simulations of transient temperature rise during acoustic radiation force-based ultrasound elastography. Ultrasound Med Biol. 2014; 40:1001–1014. [PubMed: 24548651]

Menon M, Langdon J, McAleavey S. Minimization of displacement estimation bias due to high amplitude-reflections using envelope-weighted normalization. Ultrason Imaging. 2010; 32:65–80. [PubMed: 20687275]

Muller M, Aït-Belkacem D, Hessabi M, Gennisson JL, Grangé G, Goffinet F, Lecarpentier E, Cabrol D, Tanter M, Tsatsaris V. Assessment of the cervix in pregnant women using shear wave elastography: *A feasibility study*. Ultrasound Med Biol. 2015; 41:2789–2797. [PubMed: 26278635]

Nightingale K. Acoustic radiation force impulse (ARFI) imaging: A review. Cur Med Imaging Rev. 2011; 7:328–339.

Nightingale K, Palmeri ML, Nightingale RW, Trahey GE. On the feasibility of remote palpation using acoustic radiation force. J Acoust Soc Am. 2001; 110:625–634. [PubMed: 11508987]

Nightingale K, Palmeri M, Trahey G. Analysis of contrast in images generated with transient acoustic radiation force. Ultrasound Med Biol. 2006; 32:61–72. [PubMed: 16364798]

Palmeri ML, McAleavey SA, Trahey GE, Nightingale KR. Ultrasonic tracking of acoustic radiation force-induced displacements in homogeneous media. IEEE Trans Ultrason Ferroelectr Freq Control. 2006; 53:1300–1313. [PubMed: 16889337]

Palmeri ML, Miller ZA, Glass TJ, Garcia-Reyes K, Gupta RT, Rosenzweig SJ, Kauffman C, Polascik TJ, Buck A, Kulbacki E, Madden J, Lipman SL, Rouze NC, Nightingale KR. B-mode and acoustic radiation force impulse (ARFI) imaging of prostate zonal anatomy: Comparison with 3t t2-weighted MR imaging. Ultrason Imaging. 2015; 37:22–41. [PubMed: 25060914]

Palmeri ML, Nightingale KR. Acoustic radiation force-based elasticity imaging methods. Interface Focus. 2011; 1:553–564. [PubMed: 22419986]

Palmeri ML, Sharma AC, Bouchard RR, Nightingale RW, Nightingale KR. A finite-element method model of soft tissue response to impulsive acoustic radiation force. IEEE Trans Ultrason Ferroelectr Freq Control. 2005; 52:1699–1712. [PubMed: 16382621]

Palmeri ML, Wang MH, Rouze NC, Abdelmalek MF, Guy CD, Moser B, Diehl AM, Nightingale KR. Noninvasive evaluation of hepatic fibrosis using acoustic radiation force-based shear stiffness in patients with nonalcoholic fatty liver disease. J Hepatol. 2011; 55:666–672. [PubMed: 21256907]

Parker KJ, Baddour N. The gaussian shear wave in a dispersive medium. Ultrasound Med Biol. 2014; 40:675–684. [PubMed: 24412170]

Pellot-Barakat C, Frouin F, Insana M, Herment A. Ultrasound elastography based on multiscale estimations of regularized displacement fields. IEEE Trans Med Imaging. 2004; 23:153–163. [PubMed: 14964561]

Petrank Y, Huang L, O'Donnell M. Reduced peak-hopping artifacts in ultrasonic strain estimation using the viterbi algorithm. IEEE Trans Ultrason Ferroelectr Freq Control. 2009; 56:1359–1367. [PubMed: 19574147]

Qiang B, Greenleaf J, Oyen M, Zhang X. Estimating material elasticity by spherical indentation load-relaxation tests on viscoelastic samples of finite thickness. IEEE Trans Ultrason Ferroelectr Freq Control. 2011; 58:1418–1429. [PubMed: 21768026]

Rivaz H, Boctor E, Foroughi P, Zellars R, Fichtinger G, Hager G. Ultrasound elastography: A dynamic programming approach. IEEE Trans Med Imaging. 2008; 27:1373–1377. [PubMed: 18815089]

Rouze NC, Wang MH, Palmeri ML, Nightingale KR. Robust estimation of time-of-flight shear wave speed using a radon sum transformation. IEEE Trans Ultrason Ferroelectr Freq Control. 2010; 57:2662–2670. [PubMed: 21156362]

Samir AE, Allegretti AS, Zhu Q, Dhyani M, Anvari A, Sullivan DA, Trottier CA, Dougherty S, Williams WW, Babitt JL, Wenger J, Thadhani RI, Lin HY. Shear wave elastography in chronic kidney disease: A pilot experience in nativekidneys. BMC Nephrol. 2015; 16:119. [PubMed: 26227484]

Sarvazyan AP, Rudenko OV, Swanson SD, Fowlkes JB, Emelianov SY. Shear wave elasticity imaging: A new ultrasonic technology of medical diagnostics. Ultrasound Med Biol. 1998; 24:1419–1435. [PubMed: 10385964]

Scola MR, Baggesen LM, Nichols TC, Key NS, Gallippi CM. A review of current methods for assessing hemostasis in *vivo* and introduction to a potential alternative approach. Thromb Res. 2012; 129(Suppl. 2):S57–S61. [PubMed: 22405050]

Urban MW, Chen S, Fatemi M. A review of shearwave dispersion ultrasound vibrometry (sduv) and its applications. Curr Med Imaging Rev. 2012; 8:27–36. [PubMed: 22866026]

Walker W, Trahey G. A fundamental limit on delay estimation using partially correlated speckle signals. IEEE Trans Ultrason Ferroelectr Freq Control. 1995; 42:301–308.

Zahiri-Azar R, Salcudean S. Motion estimation in ultrasound images using time domain cross correlation with prior estimates. IEEE Trans Biomed Eng. 2006; 53:1990–2000. [PubMed: 17019863]

Zhai L, Polascik TJ, Foo WC, Rosenzweig S, Palmeri ML, Madden J, Nightingale KR. Acoustic radiation force impulse imaging of human prostates: Initial *in vivo* demonstration. Ultrasound Med Biol. 2012; 38:50–61. [PubMed: 22104533]

Zhao H, Chen J, Meixner DD, Xie H, Shamdasani V, Zhou S, Robert JL, Urban MW, Sanchez W, Callstrom MR, Ehman RL, Greenleaf JF, Chen S. Noninvasive assessment of liver fibrosis using ultrasoundbased shear wave measurement and comparison to magnetic resonance elastography. J Ultrasound Med. 2014; 33:1597–1604. [PubMed: 25154941]

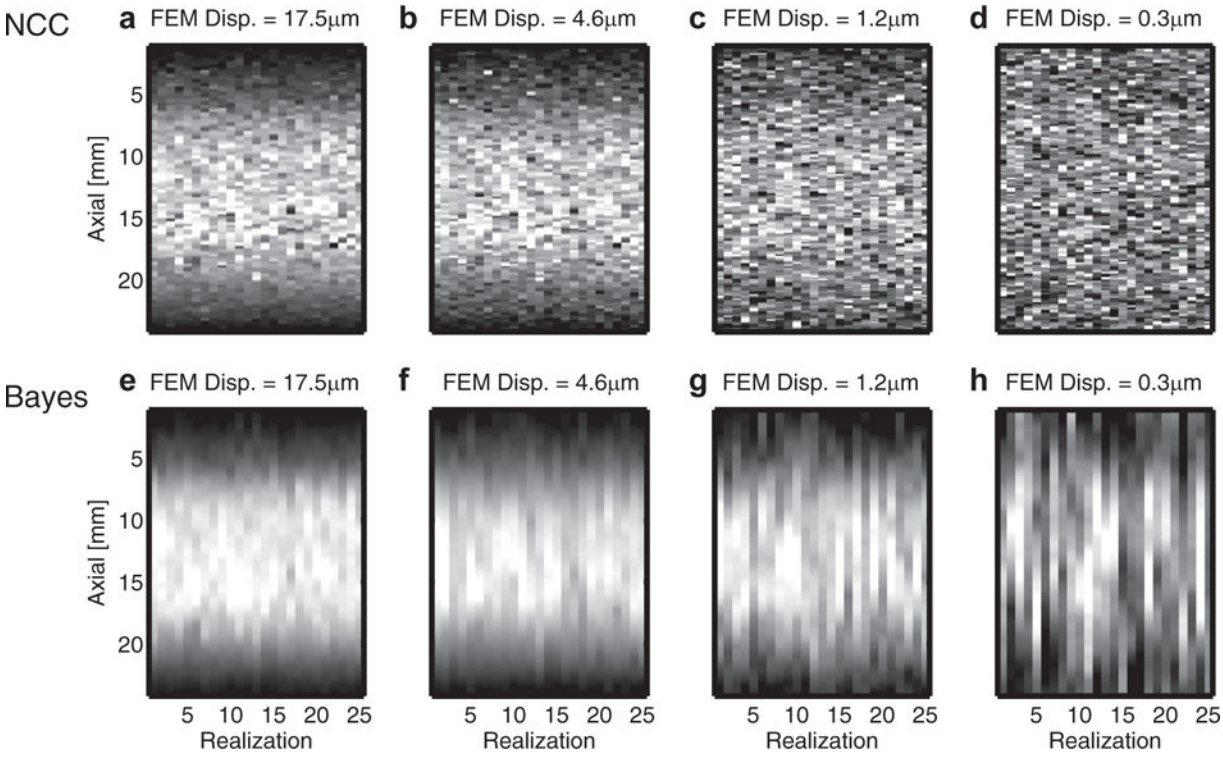


**Fig. 1.**

Peak time-step displacement profiles for every speckle realization of the simulated, homogeneous data as a function of decreasing displacement magnitude (a–d) for NCC displacements and (e–h) for Bayesian displacements. Each image is scaled to the middle 90th percentile of the data and the units are in $\mu$m. For all displacement magnitudes, the Bayesian estimator (bottom row) shows less measurement variability than the corresponding NCC images, particularly below 1 $\mu$m, where the underlying displacement profile is almost completely masked by the noise in the measurement. In contrast, the Bayesian estimator is able to almost fully recover the profile at 1.2 $\mu$m and partially recover the displacement profile at 0.3 $\mu$m. FEM = finite element model; NCC = normalized cross-correlation.

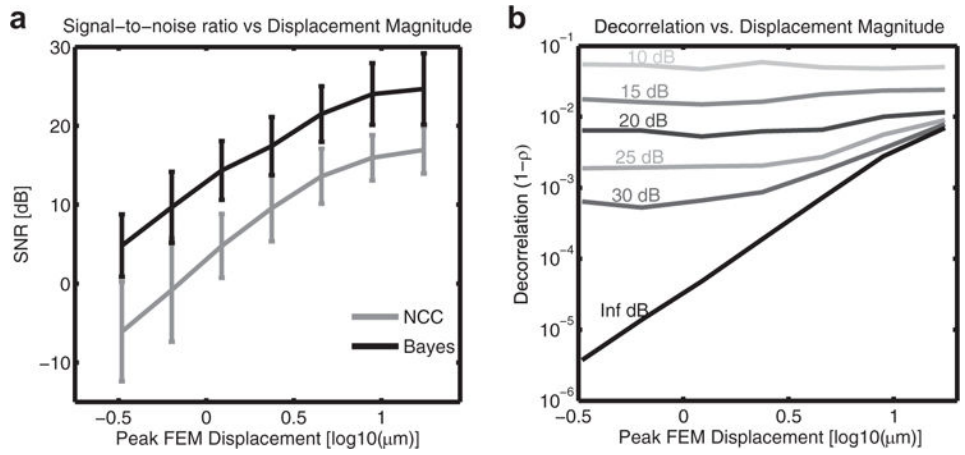


**Fig. 2.**

Peak time-step displacement SNR for the Bayesian (black) and NCC (gray) estimators as a function of peak FEM displacement ($\log_{10}$ scale) is shown in (a). The error bars show the mean and standard deviation of the SNR axially for both estimators. On average, there is an 8.9 dB improvement in displacement SNR when using the Bayesian estimator over NCC for the same displacement magnitude. The results suggest that displacement magnitude can be reduced to only a few microns when using the Bayesian estimator, without an appreciable loss in SNR relative to NCC. We also show the decorrelation at the peak focal displacement in (b). These results are shown for several SNRs to demonstrate where the decorrelation is dominated by speckle decorrelation versus thermal noise decorrelation. For smaller displacements, thermal noise is the dominant source of decorrelation, and within the domain of the conducted simulations, when thermal SNR is below 15–20 dB, it is always the primary mechanism of decorrelation. (All SNR comparisons were significant with $p$ values below $1 \times 10^{-10}$ based on a one-sided Wilcoxon rank sum test.) FEM = finite element model; NCC = normalized cross-correlation; SNR = signal-to-noise ratio.

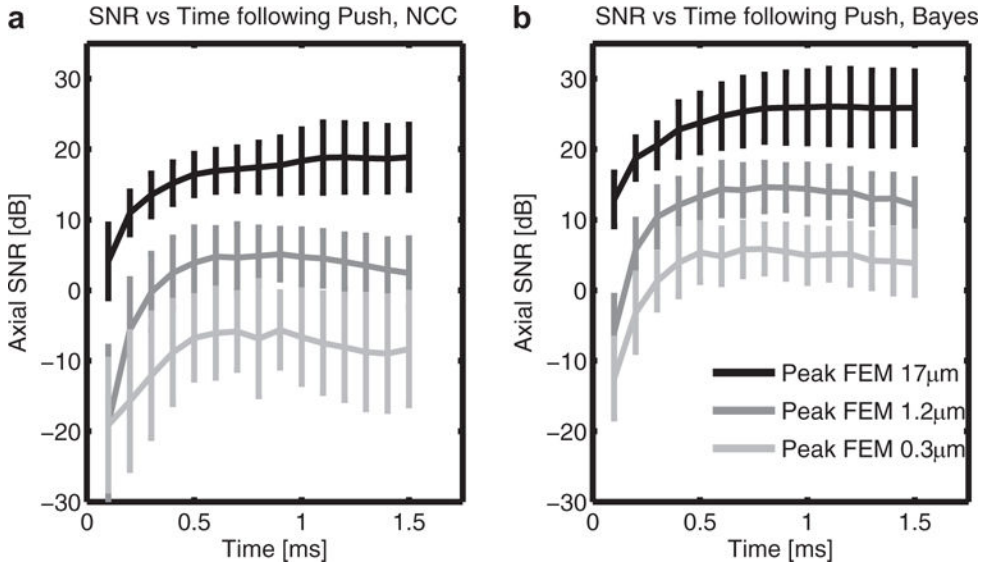


**Fig. 3.**

Displacement SNR for the NCC (a) and Bayesian (b) estimators for three peak displacement magnitude levels as a function of time following the excitation. The error bars show the mean and standard deviation of the SNR axially for both estimators. The results show the displacement SNR improvement achieved by the Bayesian estimator is maintained up to and beyond the peak-displacement time-step (t = 0.6 ms), and that this improvement occurs over the entire range of tested displacement magnitudes. (All comparisons were significant with $p$ values below $1 \times 10^{-10}$ based on a one-sided Wilcoxon rank sum test.) FEM = finite element model; NCC = normalized cross-correlation; SNR = signal-to-noise ratio.

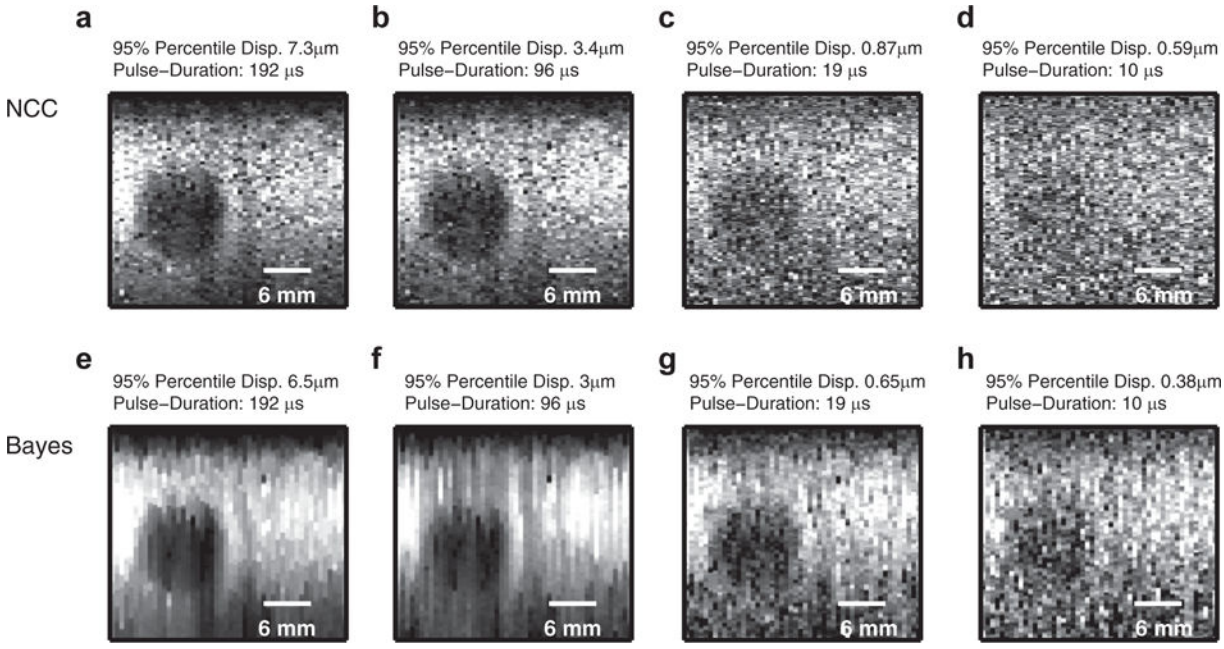


**Fig. 4.**

Example ARFI displacement images showing the 21-kPa lesion for the NCC estimator (top row; a–d) and the Bayesian estimator (bottom row; e–h) as a function of displacement magnitude and excitation pulse length. Each image is scaled to the middle 90th percentile of the data and the units are in $\mu$m. The apparent contrast of the lesion appears to be higher in the Bayesian images than the corresponding NCC images for all excitation lengths (and thus displacement magnitudes). The lesion is well visualized by the Bayesian estimator down to an excitation burst length of 19 $\mu$s, and is partially visible when the excitation is reduced to 10 $\mu$s. For the NCC estimator, the lesion is poorly resolved when the displacements fall below 1 $\mu$m. NCC = normalized cross-correlation.

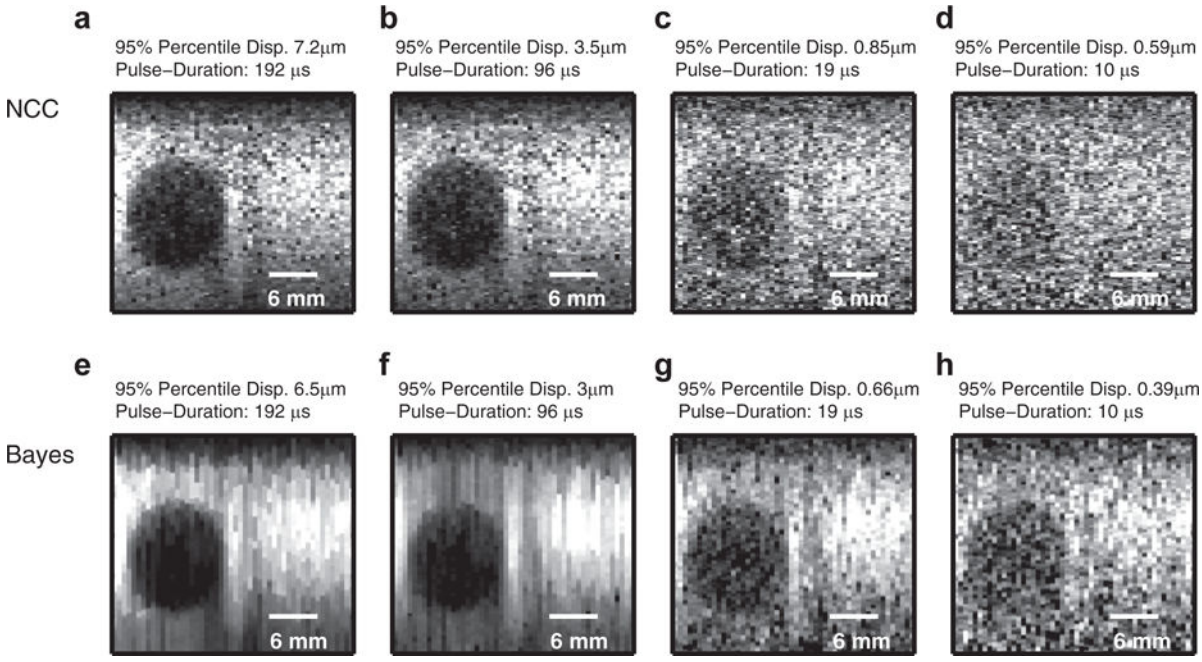


**Fig. 5.**

Example ARFI displacement images showing the 45-kPa lesion for the NCC estimator (top row; a–d) and the Bayesian estimator (bottom row; e–h) as a function of displacement magnitude and excitation pulse length. Each image is scaled to the middle 90th percentile of the data and the units are in $\mu$m. The apparent contrast of the lesion appears to be higher in the Bayesian images than the corresponding NCC images for all excitation lengths (and thus displacement magnitudes). The lesion is well visualized by the Bayesian estimator down to an excitation burst length of 19 $\mu$s, and is partially visible when the excitation is reduced to 10 $\mu$s. For the NCC estimator, the lesion is poorly resolved when the displacements fall below 1 $\mu$m. NCC = normalized cross-correlation.

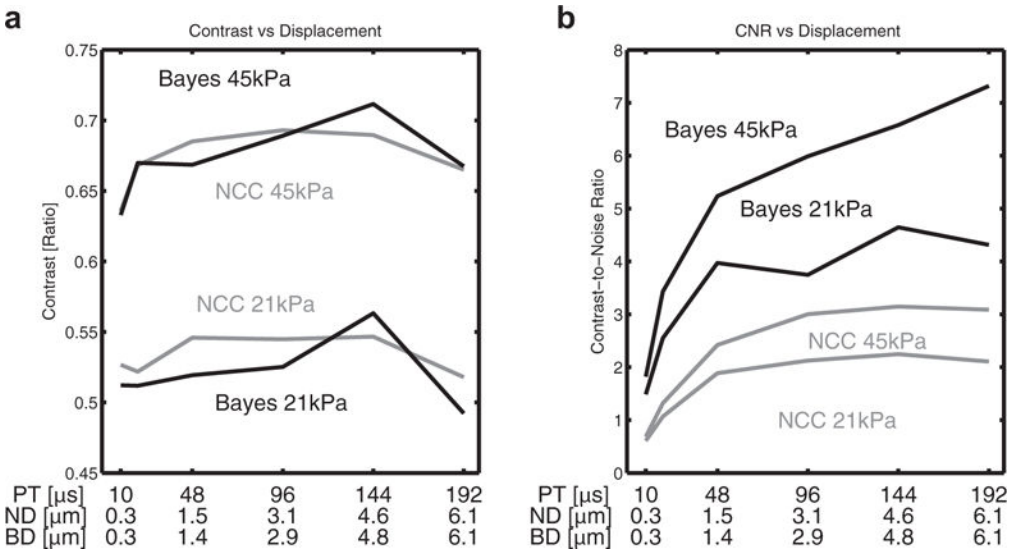


**Fig. 6.**

Contrast (a) and CNR (b) for the NCC (gray) and Bayesian (black) estimators for both lesion types. These data are plotted against the excitation pulse length (labeled PT). For reference, the mean displacement within the background region used in the analysis is also given as a function of excitation pulse length for NCC (labeled ND) and Bayesian (labeled BD) estimators. The results suggest that contrast is maintained by the Bayesian estimator, while CNR is approximately doubled relative to NCC for any given displacement magnitude. The results suggest that NCC-equivalent performance can be achieved by the Bayesian estimator at considerably smaller excitation pulse lengths and displacement magnitude levels. BD = Bayesian displacement; CNR = contrast-to-noise ratio; NCC = normalized cross-correlation; ND = NCC displacement; PT = pulse time.

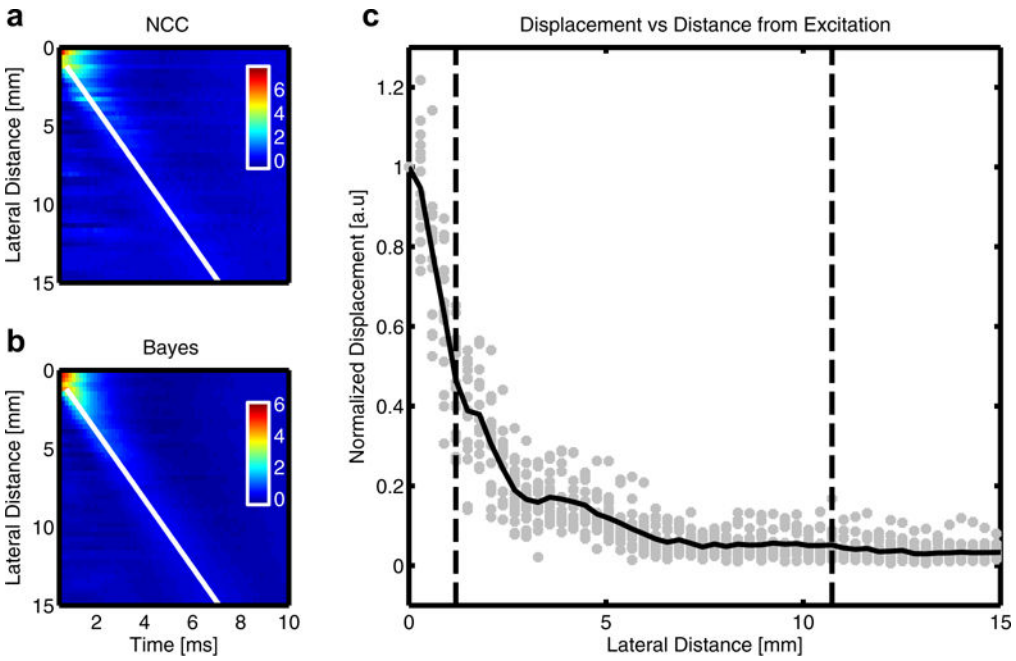


**Fig. 7.**

Focal displacement versus time and distance from the excitation source for the NCC (a) and Bayesian (b) estimators for one of the chicken breast samples. The white lines show the corresponding time-of-flight trajectories of the shear wave as computed by the Radon-sum transformation. Displacement versus distance from the excitation source (c) for data located along the time-of-flight trajectory corresponding to the peak of the propagating shear wave. The data have been normalized to the displacement within the center of the excitation region for each sample. Each gray dot shows the relative displacement from one chicken breast sample (n = 16 samples, six chicken breasts, two to three sites per breast). The black line shows mean relative displacement as a function of distance from the excitation source. The vertical dashed lines show the region used for the SNR analysis of the propagating shear wave. The first dashed line corresponds to a location just outside the initial excitation region while the second dashed line corresponds to the distance for the relative displacement of the shear wave to fall to approximately 10% of the value located at the position of the first line. NCC = normalized cross-correlation.

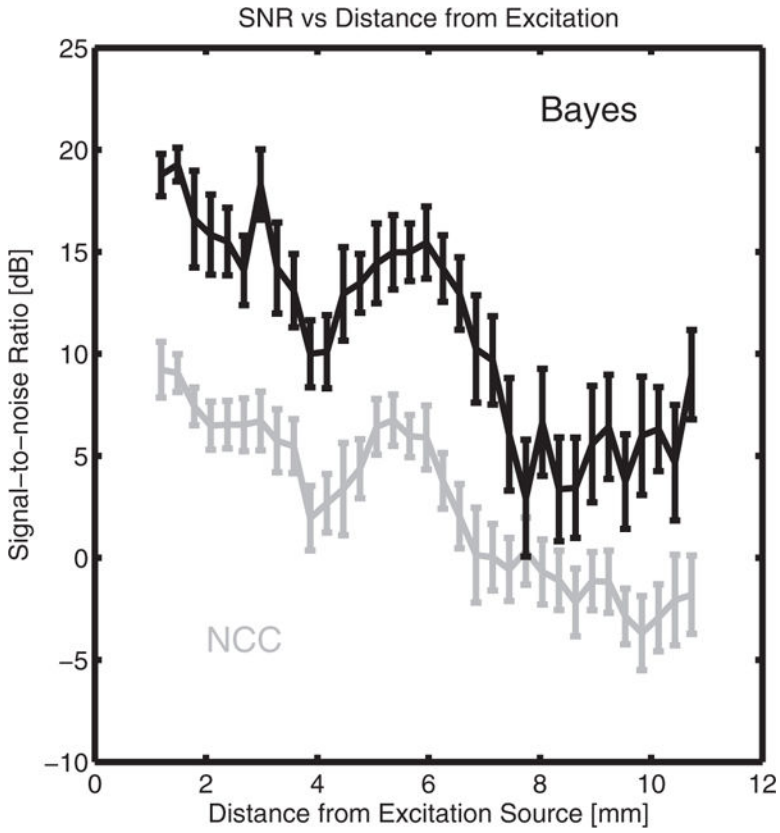


**Fig. 8.**

Displacement SNR for the chicken breast data as a function of distance from the excitation source. The images are shown in mm. The displacement SNR is calculated from a 3-mm region below the excitation focus (*i.e.*, 22–25 mm) for each sample, and represents the SNR of the peak region of the propagating shear wave. The black error bars show the mean and standard error of the mean of the data across the measurement sites (n = 16 samples, six chicken breasts, two to three sites per breast) for the Bayesian estimator. The gray error bars show the same for the NCC estimator. The results show the improvement in displacement SNR achieved by the Bayesian estimator and that this improvement is maintained throughout the measurement region. (Using a one-sided Wilcoxon rank sum test, all comparisons were significant at the $p = 0.05$ level, except distances 7.7 mm, 8.3 mm and 8.9 mm, which had $p$ values of 0.13, 0.084 and 0.068, respectively.) NCC = normalized cross-correlation; SNR = signal-to-noise ratio.

**Table 1**

ARF simulation parameters

| Parameter | Value |
|---|---|
| Attenuation coefficient | 0.5 dB/MHz/cm |
| Likelihood kernel length | $3/f_c$ |
| NCC kernel length | $3/f_c$ |
| Peak displacement | $0.3 \leq PD \leq 17.5 \mu m$ |
| Probe bandwidth | 60% |
| Probe focus | 1.2 cm |
| Samp. freq. (RF data) | 40 MHz |
| Samp. freq. (up-sampled) | 120 MHz |
| Samp. freq. (field simulation) | 1000 MHz |
| Speed-of-sound | 1540 m/s |
| Tracking frequency | 7 MHz |
| Tracking | 10 kHz |
| Up-sample factor | 3 |

ARF = acoustic radiation force; freq. = frequency; NCC = normalized cross-correlation; PD = peak displacement; RF = radiofrequency; samp. = sample.

**Table 2**

Lesion phantom experiment parameters

| Parameter | Value |
|---|---|
| Attenuation coefficient | 0.43–0.49 dB/MHz/cm |
| Background Young's modulus | 6.5 kPa |
| Lesion I Young's modulus | 21 kPa |
| Lesion II Young's modulus | 45 kPa |
| Excitation f/number | f/3 |
| Excitation ISPPA.3 | 577 W/cm$^2$ |
| Excitation mechanical index | 1.47 |
| Excitation pulse length | $10 \leq \text{EPL} \leq 192 \mu s$ |
| Likelihood kernel length | $2.7/f_c$ |
| NCC kernel length | $2.7/f_c$ |
| Number of excitations | 50 |
| Probe frequency ($f_c$) | 5.2 MHz |
| Probe focus | 2.5 cm |
| Samp. freq. (acquisition) | 21 MHz |
| Samp. freq. (up-sampled) | 125 MHz |
| Tracking | 6.7 kHz |
| Up-sample factor | 6 |

freq. = frequency; ISPPA = intensity spatial peak pulse average; EPL = excitation pulse length; NCC = normalized cross-correlation; samp. = sample.